GTP-23-1329

LARGE EDDY SIMULATION OF SOOT FORMATION IN A REAL AERO-ENGINE COMBUSTOR USING TABULATED CHEMISTRY AND A QUADRATURE-BASED METHOD OF MOMENTS

Philipp Koob[1,*], Federica Ferraro[1], Hendrik Nicolai[1], Ruud Eggels[2], Max Staufer[2], Christian Hasse[1]

[1]Technical University of Darmstadt, Departement of Mechanical Engineering, Simulation of reactive Thermo-Fluid Systems
Otto-Berndt-Straße 2, 64287 Darmstadt, Germany
[2]Rolls-Royce Deutschland Ltd. & Co. KG, Department Combustion and Turbine
Eschenweg 11, 15827 Blankenfelde-Mahlow, Germany

ABSTRACT

Considering the increasingly stringent targets for aircraft emissions, CFD is becoming a viable tool for improving future aero-engine combustors. However, predicting pollutant formation remains challenging. In particular, directly solving the evolution of soot particles is numerically expensive. To reduce the computational cost but retain detailed physical modeling, quadrature-based moments methods can be efficiently employed to approximate the particle number density function (NDF). An example is the recently developed split-based extended quadrature method of moments (S-EQMOM), which enables a continuous description of the soot particles' NDF, essential to consider particle oxidation accurately. This model has shown promising results in laminar premixed flames up to turbulent laboratory scale configurations. However, the application to large-scale applications is still scarce. In this work, the S-EQMOM model is applied to the Rolls-Royce BR710 aero-engine combustor to investigate the soot evolution process in practically relevant configurations. For this, the soot model is embedded into a high-fidelity simulation framework, consisting of large eddy simulation for the turbulent flow and mixing and the flamelet generated manifold method for chemistry reduction. An additional transport equation for polycyclic aromatic hydrocarbons is solved to model their slow chemistry and the transition from the gaseous phase to the solid phase. Simulations are performed for different operating conditions (idle, approach, climb, take-off) to validate the model using experimental data. Subsequently, the results are analyzed to provide insights into the complex interactions of hydrodynamics, mixing, chemistry, and soot formation.

*Corresponding author: koob@stfs.tu-darmstadt.de

1. INTRODUCTION

To reduce the negative impacts of hydrocarbon fuel combustion on the environment and human health, more stringent legal regulations have been imposed for aero-engine emissions. In addition to legal regulations, the aero industry has pledged to reduce pollutant emissions drastically by the year 2050 [1]. In particular, soot, resulting from the incomplete combustion of fossil-stemmed fuels (Jet A-1) or novel carbon-based sustainable aviation fuels (SAF), is one of the emission reduction goals. Understanding and predicting soot formation is crucial to fulfilling the legal requirements when developing efficient and sustainable next-generation aero-engine combustors. Besides experimental investigations, computational fluid dynamics (CFD) has become indispensable in designing new engines and reducing costs in the development phase [2]. However, simulating aero-engine combustors under realistic operating conditions remains challenging due to the interaction of complex phenomena at various scales, such as liquid injection and evaporation of the fuel, turbulence, chemical reactions at high pressures and temperatures, transient conditions, and effusion-cooled walls [3].

Since resolving all scales and physics involved remains prohibitive, efficient CFD simulations necessitate models. Due to the strong coupling of these complex phenomena, the overall modeling error is determined by the weakest model. Hence, for accurate soot predictions, a detailed soot model incorporated in a high-fidelity simulation framework is required. In aero-engine development, however, Reynolds Averaged Navier-Stokes simulations (RANS) with simplified models, such as the two-equation soot model [4], are considered industry standards in design development [3]. Studies with semi-empirical approaches [5, 6], but also more detailed soot models applied to research combustors [7–9] reported that predicting soot was challenging. These models lack generality and are mostly limited to specific fuels and operating conditions different from those in aero engines [10–

12]. Additionally, experimental results of the real engine are limited, making in-depth validation challenging. Only few works have investigated soot formation in practically-relevant gas turbine combustors using advanced numerical models [13, 14]. For high-fidelity simulations, a detailed representation of the flow field and mixing field by means of scale-resolved simulations is of great importance. Here, direct numerical simulations (DNS) remain prohibitive in the context of complex geometries. However, large eddy simulations (LES) overcome this issue by only resolving the large scales, while the smaller scales are modeled with a suited sub-grid scale model [15]. Similarly, sufficiently large kinetic mechanisms are required to describe complex fuels, their conversion, and the formation of soot precursors. The direct integration of such kinetics into CFD renders simulations exceptionally computationally expensive. Flamelet-based modeling, such as the Flamelet Generated Manifold (FGM) method [16], are popular for combustion modeling with LES due to their capabilities to resolve flame structures with detailed kinetic mechanisms at reduced computational costs. First results of flamelet LES coupled with a detailed soot model [13] showed promising results, demonstrating that scale-resolving simulations with advanced pollutant models are desirable for aero-engine simulations.

One primary reason that hinders the use of detailed soot models in CFD simulations is that the formation and evolution of soot are governed by the high-dimensional population balance equation (PBE), which is numerically expensive to solve. Therefore, efficient methods to approximate the PBE, such as the Methods of Moments (MOM) [17–21], were recently developed to characterize the particle number density function (NDF) in turbulent reacting flows. In the methods of moments, the particle NDF is not solved directly but is approximated by solving transport equations for its lower-order statistical moments. Based on these moments, an inversion algorithm is used to reconstruct the unknown NDF [22, 23]. The solution of only a few transport equations makes this method effective and is therefore suited to be used in combination with reactive scale-resolving LES. However, describing the oxidation of the smallest particles with the classic MOM remains challenging as pointwise and discrete information on the NDF is not available [24]. Out of the different quadrature-based moment closures, the Extended Quadrature Method of Moments (EQMOM) [25] overcomes this problem and provides a continuous reconstruction of the NDF by an approximation with a set of kernel density functions (KDF). This method has proven to be particularly suited for predicting soot particle formation, growth and oxidation [26]. However, the iterative and non-unique inversion algorithm applied in this method makes the inclusion in three-dimensional simulations challenging [25, 27, 28]. The recently developed Split-based Extended QMOM (S-EQMOM) approach overcomes these numerical difficulties by approximating the unknown NDF by a sum of coupled sub-NDFs of known shape [24]. Instead of solving for the moments of the whole NDF, the low-order moments of the sub-NDFs are used. Here, the advantage is that the inversion algorithm provides a set of equations with a unique solution for the moment inversion resulting in a robust method for reconstructing the soot particle NDF. The accuracy of the S-EQMOM was hierarchically validated from laminar premixed flames at highly oxidating conditions [24] over a turbulent jet flame [29] up to a single sector model combustor at elevated pressure [30]. Promising results were achieved in these laboratory configurations, which makes the method desirable for large-scale aero engines with challenging environments, such as multi-phase flows and high pressures.

In this work, flamelet LES at realistic operating conditions of the Rolls-Royce BR710 annular aero-engine combustor are performed in combination with the S-EQMOM. First numerical investigations of this combustion chamber were performed for NO_x prediction and reduction in the late 90s [31, 32]. Recently, Eigentler et al. [14] investigated soot formation in this combustor using RANS simulations with finite rate chemistry, a sectional model for soot precursors, and a two-equation soot model.

The objective of this work is to characterize soot formation and evolution in a realistically operated aero-engine combustor using the recently developed S-EQMOM soot model incorporated in a high-fidelity simulation framework. First, the resulting flow fields are analyzed and soot emissions are validated with the available experimental data. The soot particle size distribution (PSD) inside the aero-engine combustor is then reconstructed for the first time, enabling a deeper understanding of particle formation and evolution inside the rich, quench, and lean regions of the combustion chamber at four characteristic aircraft operating conditions, idle, approach, climb, and take-off.

2. NUMERICAL MODELS AND SETUP

In this section, the numerical framework and the models that enable the simulation of aero-engines are first given. Then, the numerical setup, including the computational domain and the applied boundary conditions, is presented.

2.1 Simulation Framework

CFD. The simulations are performed using the CFD solver PRECISE-UNS developed and maintained by Rolls-Royce [33]. The code is a cell-based finite volume solver specialized for the simulation of aero-engine combustors. It uses a pressure-based algorithm to solve the Favre-averaged Navier-Stokes equations in the low Mach number formulation. All diffusive fluxes and the pressure correction equation are discretized using second-order central differences and the convective fluxes are discretized with a second-order variation diminishing scheme [34]. Second-order backward differences are used to discretize unsteady terms. In the context of LES, the computational grid acts as a spatial filter. The non-resolved subgrid viscosity is modeled using the σ-model by Nicoud et al. [35] with a model constant of $C_\sigma = 1.35$. A Lagrangian particle tracking method is used to describe the evolution of the fuel spray. The fuel is injected at prescribed locations with droplet diameters sampled from a Rosin-Rammler distribution with prescribed statistical properties and a steady-state evaporation model is applied [36]. The resulting spray distribution is

assumed to correspond to the distribution after the atomization.

Combustion Model. The evolution and formation of soot are strongly connected to the gas phase chemistry. Hence, detailed information on the thermo-chemical state, such as species concentration and temperature, is required for an accurate prediction. Detailed kinetics of the combustion process are desired but not applicable due to the increased computational costs. The Flamelet Generated Manifold (FGM) approach [16] used in this work allows using detailed kinetics at a reduced cost for large-scale simulations. Instead of solving the entire thermo-chemical state during the simulation, freely-propagating premixed flamelets with varying mixture fractions are calculated in a preprocessing step. The flamelets are calculated with the one-dimensional flame solver `CHEM1D` [37]. The kerosene fuel (Jet-A1) is represented by a surrogate consisting of 52 vol-% dodecane ($C_{12}H_{26}$), 15.8 vol-% iso-octane (C_8H_{18}), 12.1 vol-% cyclohexane (C_6H_{12}), and 20.1 vol-% trimethylbenzene (C_9H_{12}). The chemical kinetics are modeled with a recently developed mechanism for kerosene surrogates specialized for soot formation [38, 39], which is based on a multicomponent reaction mechanism [40]. Subsequently, the calculated flamelets are parameterized by the mixture fraction Z and the progress variable Y_C and stored in a manifold. The progress variable is defined as $Y_C = Y_{CO_2} + Y_{CO} + Y_{H_2O} + Y_{H_2}$. The subgrid-scale turbulence-chemistry interaction is taken into account by a presumed probability density function (PPDF) approach [3]. This adds the variances Z''^2 and $Y_C''^2$ as additional control variables, leading to a four-dimensional manifold for the characterization of the thermo-chemical state. 200 flamelets inside the flammability limits of kerosene were used for the tabulation. For the tabulation, 400 points were used for the mixture fraction and 100 for the progress variable. Ten points were used for both variances to discretize the respective PDF. A stretched grid with increased resolution towards lower values was used for the mixture fraction and its variance to minimize interpolation errors during the table access. For each control variable, a transport equation is solved

$$\frac{\partial \bar{\rho}\tilde{\phi}}{\partial t} + \frac{\partial \left(\bar{\rho}\tilde{u}_i\tilde{\phi}\right)}{\partial x_i} = \frac{\partial}{\partial x_i}\left(\bar{\rho}\left[\frac{\bar{\nu}}{Sc} + \frac{\nu_T}{Sc_T}\right]\frac{\partial \tilde{\phi}}{\partial x_i}\right) + \tilde{q} + \bar{S}_{sp} \quad (1)$$

with $\phi = \left[Z, Y_C, Z''^2, Y_C''^2\right]$, the general source term of the transport equation q, the spray source term S_{sp}, the viscosity ν, the Schmidt number Sc, the turbulent viscosity ν_T, and the turbulent Schmidt number Sc_T. The local thermo-chemical state according to the control variables is retrieved from the FGM table.

Soot Model. The evolution of soot precursors in the gas phase is captured by the FGM model presented in the previous section. For the transition into the solid phase and further development of soot particles, the S-EQMOM model [24] is applied in this work. The S-EQMOM model approximates the unknown soot NDF $n(x_i, t; \boldsymbol{\xi})$ by a set of coupled sub-NDFs $n_{s_l}(x_i, t; \boldsymbol{\xi})$, where s_l is the index of the sub-NDF. Here, soot particles are considered to be spherical and are described only by their volume V. Therefore the vector of the internal coordinates is $\boldsymbol{\xi} = [V]$. Gamma distributions are used to approximate the soot particle NDF, following [24, 26]. To account for the evolution of each sub-NDF, transport equations for their three lower-order moments, $k = 0, 1, 2$, need to be solved

$$\frac{\partial \bar{m}_k(x_i,t)}{\partial t} + \frac{\partial \tilde{u}_i \bar{m}_k(x_i,t)}{\partial x_i} = \frac{\partial}{\partial x_i}\left(D_T \frac{\partial \bar{m}_k(x_i,t)}{\partial x_i}\right) + \bar{\dot{m}}_k. \quad (2)$$

Here, m_k stands for the k-th moment, u_i for the i-th velocity component and $D_T = \nu_T / Sc_T$ for the turbulent diffusivity with the turbulent Schmidt number Sc_T set to 0.7. The source terms $\dot{m}_k$ of the moment equations include particle formation through nucleation from PAH molecules, coagulation, surface growth by condensation, the hydrogen abstraction/acetylene addition (HACA) mechanism and particle oxidation. Describing chain-like aggregates requires an additional particle property, e.g., the particle surface. Therefore, soot aggregation is currently not considered in the model, similar to [41]. Nucleation is modeled by a dimerization reaction of two pyrene molecules [42]. Coagulation is modeled following Kazakov and Frenklach [43]. Surface growth through condensation is modeled by the collision of pyrene molecules with soot particles [42]. Chemical surface growth is modeled with the HACA mechanism [44, 45]. Oxidation of soot particles is assumed to take place through reactions with O_2 and OH [45]. The rates for the HACA mechanism and oxidation are taken from [46]. Two sub-NDFs are used in this work, similarly to [24, 29], leading to six additional moment transport equations. The details of the S-EQMOM model and the source terms are presented in [24] and are not repeated here for brevity. To take into account the slow PAH chemistry and the mass transfer from the gaseous into the solid phase, an additional filtered transport equation for the PAH mass fraction is introduced [19]

$$\frac{\partial \bar{\rho}\tilde{Y}_{\mathrm{PAH}}}{\partial t} + \frac{\partial \bar{\rho}\bar{u}_i\tilde{Y}_{\mathrm{PAH}}}{\partial x_i} = \frac{\partial}{\partial x_i}\left[\bar{\rho}\left(D_e\right)\frac{\partial \tilde{Y}_{\mathrm{PAH}}}{\partial x_i}\right] + \bar{\dot{\omega}}_{\mathrm{PAH}}, \quad (3)$$

with $D_e = D + D_T$ the effective diffusion coefficient, D the molecular diffusion coefficient.

Pyrene ($C_{16}H_{10}$) is considered as the PAH soot precursor and is used for $\tilde{Y}_{\mathrm{PAH}}$. Following [19, 47], to model the slow chemistry of PAH, the filtered source term $\bar{\dot{\omega}}_{\mathrm{PAH}}$ is split into three different components: a chemical production term $\bar{\dot{\omega}}^{+}_{\mathrm{PAH}}$ independent of the gas phase, a chemical destruction term $\bar{\dot{\omega}}^{-}_{\mathrm{PAH}}$ that is linear dependent on the PAH mass fraction, and a consumption term $\bar{\dot{\omega}}_s$ representing the mass transfer from the gas phase to solid phase through nucleation of PAHs, which is quadratic to the species mass fraction

$$\bar{\dot{\omega}}_{\mathrm{PAH}} = \bar{\dot{\omega}}^{+T}_{\mathrm{PAH}} + \bar{\dot{\omega}}^{-T}_{\mathrm{PAH}}\left(\frac{\tilde{Y}_{\mathrm{PAH}}}{\tilde{Y}^{T}_{\mathrm{PAH}}}\right) + \bar{\dot{\omega}}^{T}_{s}\left(\frac{\tilde{Y}_{\mathrm{PAH}}}{\tilde{Y}^{T}_{\mathrm{PAH}}}\right)^2. \quad (4)$$

The superscript T denotes that the value is taken from the FGM table. The remaining quantities are directly used from the transport equation.

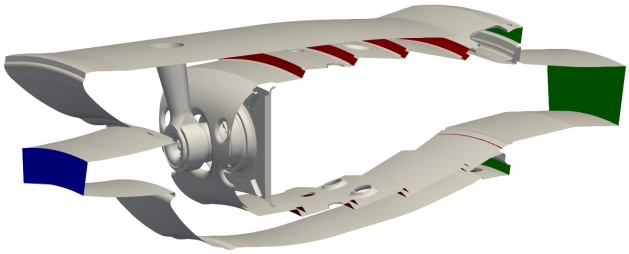

FIGURE 1: COMPUTATIONAL DOMAIN WITH HIGHLIGHTED INLET (1), OUTLET (3) AND EFFUSION COOLING BOUNDARY CONDITIONS (2).

2.2 Geometry and Boundary Conditions

In this work, the Rolls-Royce BR710 aero-engine combustion chamber is investigated. This combustion chamber follows the rich-quench-lean (RQL) concept with a rich mixture in the primary reaction zone, fast quenching through mixing with fresh air, and a lean region towards the exit. To reduce the computational effort, only a segment of 18° of the annular combustion chamber, including one fuel injector, is simulated with periodic boundary conditions in the circumferential direction. The computational domain includes all important geometrical features, such as the fuel injector and the outer parts of the combustion chamber for the annulus airflow, and is shown in Fig. 1. The fuel injection is modeled by a spray located near the edge of the prefilming airblast atomizer with a prescribed Sauter mean particle diameter, initial velocity, and fuel mass flow rate. To prevent overheating, the combustion chamber walls are cooled by Z-ring cooling, in which fresh air is injected through holes. These holes are not resolved since this would increase considerably the number of cells. Therefore, an effusion cooling boundary condition with a uniform mass flow rate is applied to these regions. This boundary condition models the injection or suction of the fluid flow through the boundary by mass source terms in the governing equations. Fresh air enters the computational domain at the inlet (Blue patch Fig. 1) with an operating point specific mass flow and temperature. The annulus air and exhaust gases leave the domain through four exits with zero gradient boundary conditions (Green patch Fig. 1). The computational domain is discretized by approximately 5.5 million cells, consisting of predominantly hexahedral cells in the core and polyhedral cells towards the walls. A mesh refinement is applied in the region of the injector and the primary reaction zone as well as at the dilution holes. The quality of the mesh was estimated using the IQ_ν criterion introduced by Celik et al. [48]. Inside the combustion chamber, values

TABLE 1: OPERATING CONDITIONS

	take-off	climb	approach	idle
thrust level	100 %	85 %	30 %	7 %
w_{ff} in gs^{-1}	35.71	29.74	10.72	4.46

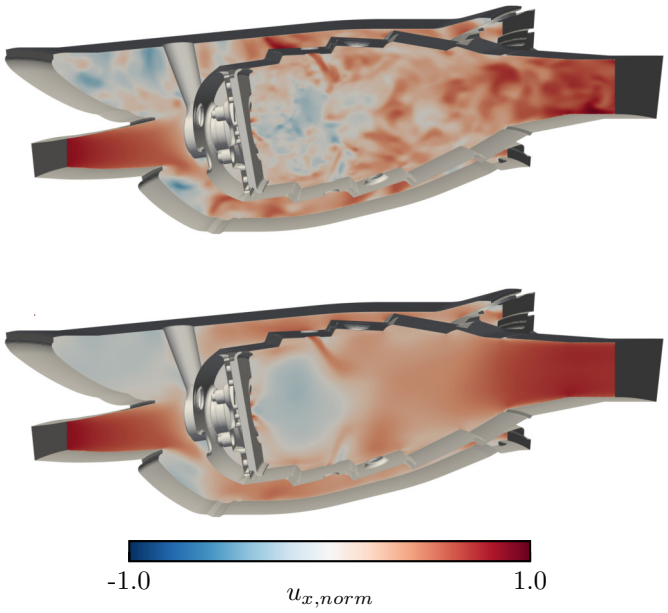

FIGURE 2: INSTANTANEOUS (TOP) AND MEAN (BOTTOM) AXIAL VELOCITY FOR THE TAKE-OFF OPERATING CONDITION.

> 80 % are achieved in the main region of interest and values > 70 % for the rest. To evaluate the performance of the model over the entire operating range of the engine, simulations of four operating conditions are performed and validated based on the soot measurements available in the International Civil Aviation Organization (ICAO) engine certification data bank [49]. The corresponding thrust levels and fuel mass flows w_{ff} are shown in Tab. 1. With higher thrust levels, the operating pressure and inlet temperature are continuously increased while the air-fuel ratio (AFR) is decreased.

3. RESULTS AND DISCUSSION

For all operating conditions presented in the previous section, LES with the S-EQMOM soot model were performed. The computational cost for each operating point is about 270.000 core hours per 0.1 s physical simulation time. In this section, the results of these simulations are presented and analyzed.

Global Characteristics of the Combustion Chamber. The normalized instantaneous and mean axial velocity component for the take-off operating point is shown in Fig. 2. Normalization is achieved by dividing the velocity by its value at the combustor exit. The incoming fresh air is split into different paths when entering the combustor. Part of the air enters the combustion chamber through the injector and heatshield. The remaining air flows through the annuli and subsequently via the mixing and cooling holes into the combustion chamber. The instantaneous velocity features significant fluctuations in all parts of the combustion chamber. The swirled flame stabilizes in the primary reaction zone and a characteristic inner recirculation zone is formed be-

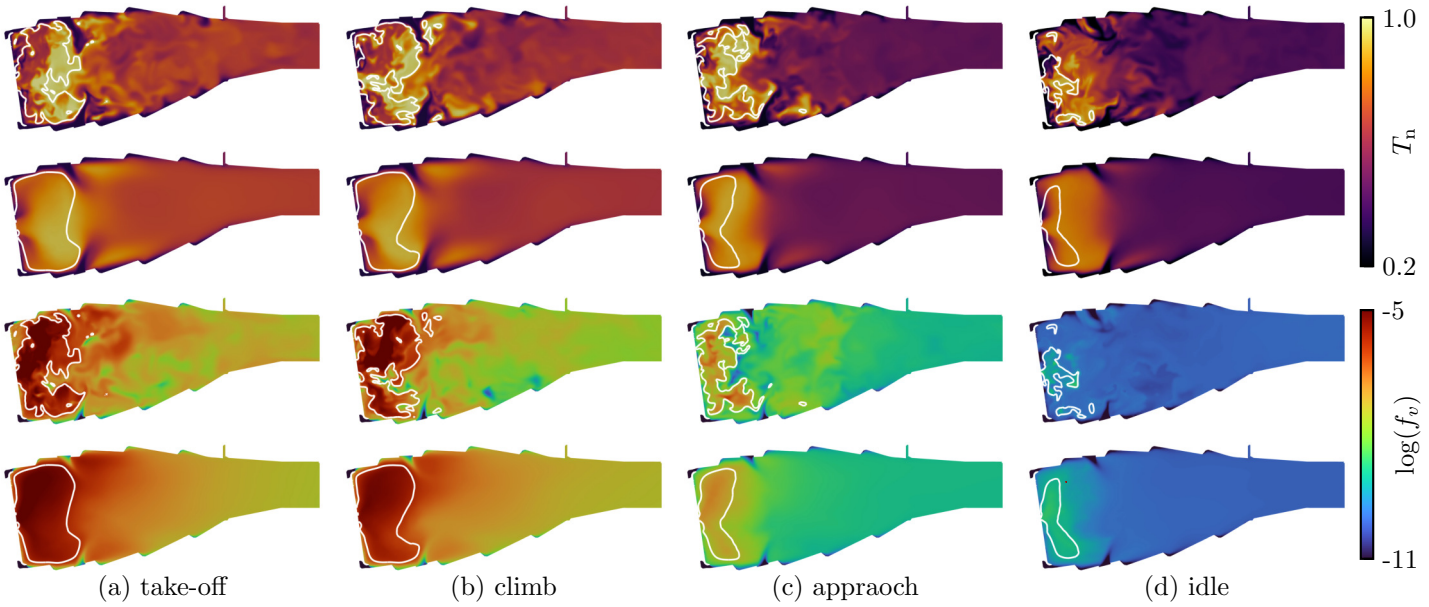

FIGURE 3: INSTANTANEOUS (TOP) AND MEAN (BOTTOM) NORMALIZED TEMPERATURE AND SOOT VOLUME FRACTION f_v FOR TAKE-OFF (a), CLIMB (b), APPROACH (b) AND IDLE (d) CONDITION. THE WHITE LINE REPRESENTS THE STOICHIOMETRIC MIXTURE FRACTION ISOLINE.

hind the injector. The rich mixture is then quenched and diluted with fresh air entering the combustion chamber through mixing holes. Two jets are visible in the plane shown in Fig. 2, but more mixing holes are present outside of the depicted plane. Towards the exit, the burned exhaust gases are accelerated through the constriction of the geometry and thermal expansion. The velocity field for the other three operating conditions is similar to the highest load case and omitted here for brevity. While the velocity field is very similar for all four operating conditions, significant differences can be observed in the mixing fields and the temperature distribution. For improved visualization and as the main focus of this work is on the soot formation inside the combustion chamber, all figures shown in the following are restricted to the combustion chamber. The instantaneous normalized temperature shown in Fig. 3 is the highest in the rich fuel zone. Normalization is achieved by dividing the temperature with the highest present temperature. While the two highest thrust levels have very similar temperature distributions, a significant change can be observed between the climb and approach cases. The temperatures in the quenching zone and the combustor exit are significantly reduced due to the higher AFR at lower operating conditions. While the regions of the highest temperatures are located inside the recirculation zone for the two higher load cases, they move towards the combustor walls for the lower ones. The peak temperature is also decreasing with lower thrust levels. The fuel-rich zone inside the white iso-line of the stoichiometric mixture fraction decreases continuously from take-off to idle. An asymmetry of the mean mixture fraction can be seen for all operating points. The injector and the combustion chamber center line are tilted relative to the rotation axis of the engine and the annulus airflow is asymmetric as well. Especially in the upper annulus airflow, a Kármán-like vortex street is formed behind the stem of the injector and therefore induces fluctuations in the flow through the dilution hole located in line with the stem. Additionally, the flow through the outer swirlers of the injector is also affected by it and results in an asymmetric flow at the injector exit. This can also be seen in the instantaneous axial velocity component in Fig. 2. These geometrical features and flow fluctuations influence the mixing behavior inside the combustion chamber and lead to an asymmetric flow field. This asymmetric behavior has not been published before. Previous studies using a simplified setup with modeled inflow conditions for the swirled flow through the injector and the dilution holes show a symmetric flow field [14, 31].

Differences between the operating conditions also occur for the soot volume fraction f_v depicted in the two bottom rows of Fig. 3. Similar to the temperature, no significant changes are visible between take-off and climb conditions. In contrast, the soot volume fraction is reduced by several orders of magnitude for the approach and idle conditions. For all cases, the maximum soot volume fraction is reached in the primary reaction zone at rich mixtures. The instantaneous distribution of the soot volume fraction strongly correlates with rich mixtures for all operating conditions. Especially in the quench zone of the combustor, near the dilution holes, the formation of "soot pockets" with high soot volume fraction can be observed. These pockets are formed in regions of high mixture fraction and then transported further downstream towards the exit. Simultaneously, the dilution with fresh unburned air leads to oxidation and therefore a continuous

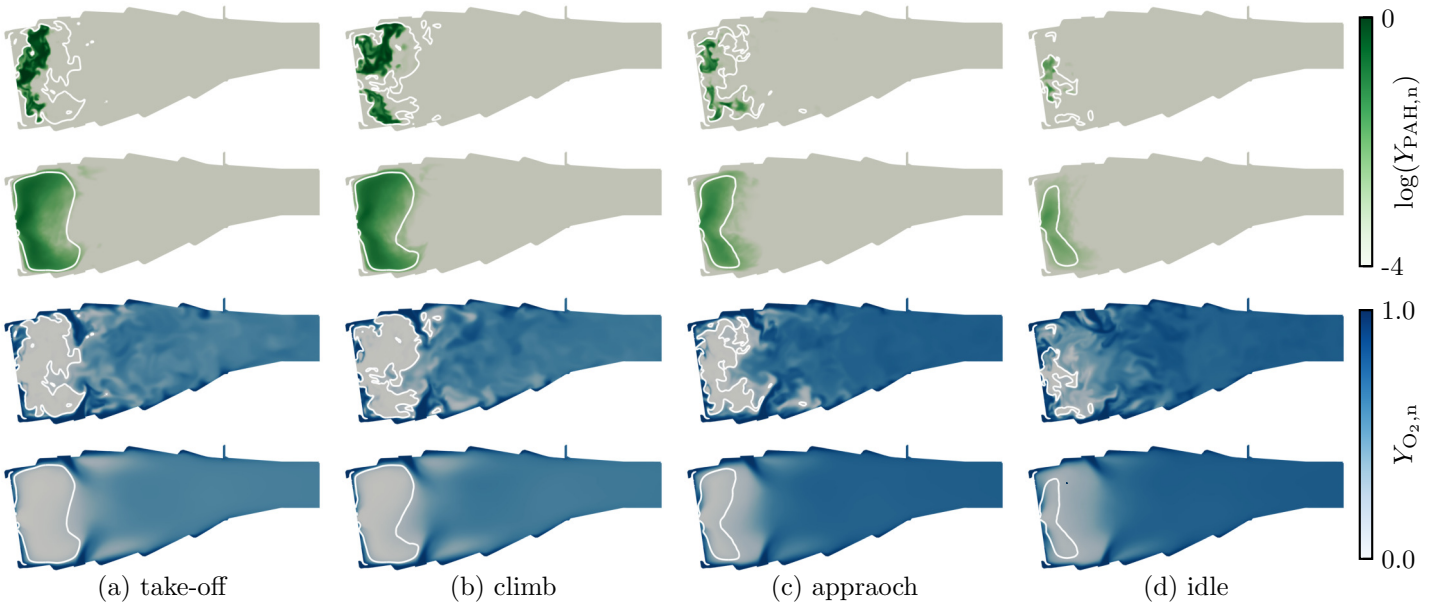

FIGURE 4: INSTANTANEOUS (TOP) AND MEAN (BOTTOM) NORMALIZED PAH MASS FRACTION AND NORMALIZED O_2 MASS FRACTION FOR TAKE-OFF (a), CLIMB (b), APPROACH (b) AND IDLE (d) CONDITION. THE WHITE LINE REPRESENTS THE STOICHIOMETRIC MIXTURE FRACTION ISOLINE.

decrease of soot, including these pockets. This behavior holds for all investigated operating conditions. The evolution of soot is driven by counteracting processes, i.e., nucleation and oxidation. These two processes are driven by the gas phase mixture composition: PAH and O_2 mass fraction for nucleation and oxidation, respectively. The normalized mass fraction of these species is shown in Fig. 4. The PAH mass fraction in the top part and the O_2 mass fraction in the bottom part of the figure are normalized with the maximum value of the respective species mass fraction. PAH is predominantly formed in very rich zones close to the injector nozzle. However, the mean fields indicate significantly lower values that span a larger area than the instantaneous fields. This indicates a strong transient behavior, which would be challenging to capture in steady simulations. Similar to the soot volume fraction, the PAH mass fraction is reduced by approximately two orders of magnitude for the idle case compared to the take-off condition in the primary reaction zone. The O_2 mass fraction represented in the bottom part follows the RQL concept. In the rich zone, the oxygen is consumed by the combustion. Hence, pockets and regions of void oxygen are formed and transported far downstream of the combustor. In the quench and lean zone, a significant increase in the oxygen fraction is observed. While the mean fields are very similar for all four conditions, more O_2 is found for the lower operating conditions due to higher AFRs.

Soot Emissions. Experimental investigations in aero-engine combustors under realistic high-pressure conditions are usually very challenging to perform and detailed results are only sometimes publicly available. However, due to legal requirements for the certification, the publication of engine data, especially for emissions, is required. In addition to CO and NO_x emissions, particle emissions must also be listed. One of these parameters for comparison is the mass-based emission index EI_{mass}. It gives the amount of soot at the exit of the combustor in relation to the fuel mass flow in mg soot per kg fuel

$$EI_{\text{mass}} = \frac{\dot{m}_{\text{soot}}}{\dot{m}_{\text{fuel}}}. \tag{5}$$

The certification data is taken from the ICAO database [49]. In the simulations, the emission index is calculated at the exit of the computational domain at every time step. The temporal evolution of the emission index shows large fluctuations up to one order of magnitude for all cases, see Fig. 5 (a). Especially for the two highest load cases (climb and take-off) large scale fluctuations with high absolute values are observed. These fluctuations are caused by the unsteady formation and oxidation of soot pockets in the quench region of the combustion chamber, which are transported downstream to the exit of the combustor. Due to these fluctuations, very long simulation runtimes are required to sample enough data for representative mean values. A quantitative comparison of the mean value for all four operating conditions and the experimental data is shown in Fig. 5 (b). The mean values are calculated over a time period of 0.1 s. The trend and values of the experiments are captured favorably. In particular, a good agreement is obtained for the idle and the climb case. At the take-off and approach condition, the soot emissions are slightly underestimated.

Particle Size Distribution. One of the main advantages of the applied S-EQMOM soot model over classical moment meth-

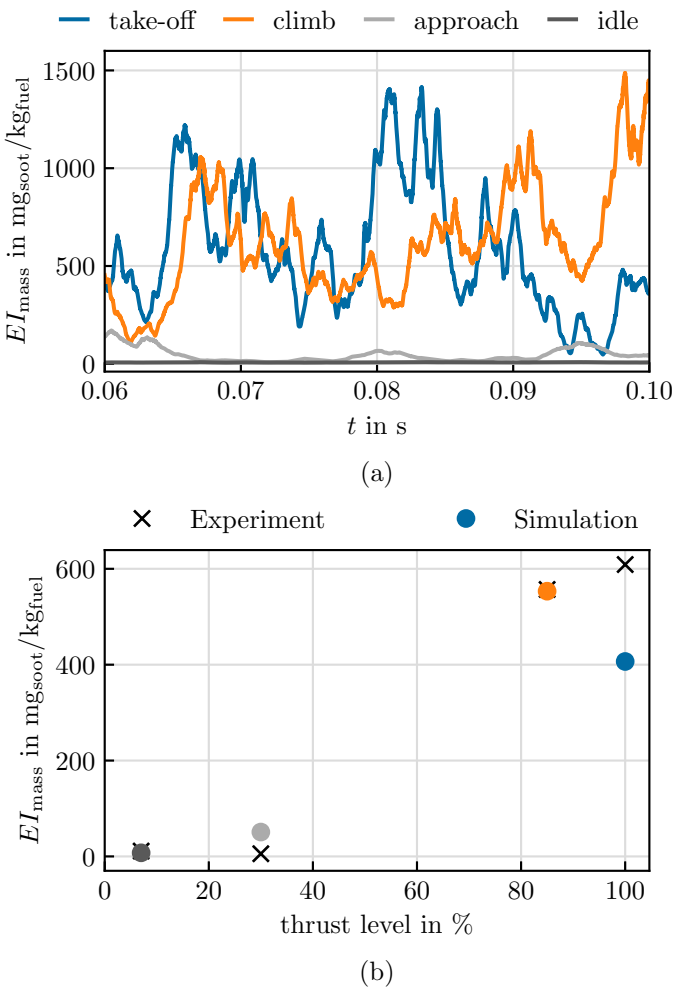

FIGURE 5: MASS BASED SOOT EMISSION INDEX FOR THE FOUR SIMULATED OPERATING CONDITIONS, TEMPORAL FLUCTUATION OF THE EMISSION INDEX (a) AND COMPARISON TO THE CERTIFICATION DATA (b).

ods is the availability of spatial and temporal information on the reconstructed PSD. In the following, the reconstructed PSD in different zones (i.e., rich, quench, and lean zone) of the combustor for all four operating conditions is investigated. Figure 6 shows the mean PSD of all four investigated operating conditions in different regions of the combustion chamber. To calculate the mean PSDs, two-dimensional slices of the instantaneous flow field of the combustion chamber are taken into account. The rich region (a) consists of the primary reaction zone in front of the mixing holes, the quench region (b) covers the part of the combustor where the fresh air gets mixed with the burned gases and includes both rows of mixing holes and the lean zone (c) was sampled near the outlet of the combustion chamber.

In the rich region, first soot particles are formed and the highest number of small particles is expected to be found. For the approach, climb and take-off condition, the PSD shows a bimodal distribution with a high density of small particles. In contrast, for the idle condition, the PSD exhibits an unimodal distribution. For this case, the PAH concentration is very low compared to the other cases (see Fig. 4) and therefore less soot and no large particles are found. The two highest load cases, climb and take-off, show very similar results for the particle size distribution with a peak of incipient small particles and the formation of large particles due to surface growth and coagulation. Furthermore, the maximum particle diameter decreases with reduced thrust and is in line with the results obtained for the soot volume fraction (see Fig. 3). In the quenching region (b), the abundance of oxygen injected through the mixing holes favors oxidation and the overall number of particles is reduced at all operating conditions while the maximum particle diameter remains constant. For the climb and take-off condition, similar PSDs are obtained. The bimodal shape of the PSDs is maintained for all operating conditions except the idle case, where the shape is still unimodal.

When moving further downstream into the lean region (c) of the combustor, the particle number density reduces significantly for all operating conditions. With longer residence times in regions with ample oxygen, the effect of oxidation becomes more prominent. The two lower thrust operating points, idle and approach, have a bimodal-shaped distribution with a lower particle density for all particle diameters compared to the PSD in the rich region. The bimodal shape is seen for the first time in this region for the idle condition. In particular, particles with a diameter larger than 10 nm have a particle density lower than $10^9\,\mathrm{cm}^{-3}$, showing substantial particle oxidation. Note that for the idle case, the particle density for the smallest particles is only slightly decreased and higher than for the approach condition. This can be related to lower temperatures but similar residence times that slow down the particle oxidation. Contrary, the two higher load cases exhibit a dominant second mode with larger particles with diameters up to 200 nm. Overall, the particle number is reduced by several orders of magnitude over the entire particle diameter space compared to the value in the upstream region. Since very large particles are harder to oxidize due to short residence times in the quench and lean zone, their particle number decreases slower compared to small particles. At the take-off condition, a slightly lower soot particle density than for the climb case is observed, although it is higher in the rich and quenching regions. This agrees with the previously shown results for EI_{mass} calculated at the combustor exit, where the take-off condition exhibits lower values compared to the climb condition.

4. CONCLUSION

In this work, soot formation and evolution of the Rolls-Royce BR710 aero-engine combustor at four relevant operating conditions have been simulated with an advanced soot model embedded into a high-fidelity LES framework. The recently developed S-EQMOM soot model has been applied with the FGM method for combustion modeling and the presumed PDF approach for turbulence chemistry interaction. An additional transport equation for the lumped PAH species was included to take the coupling

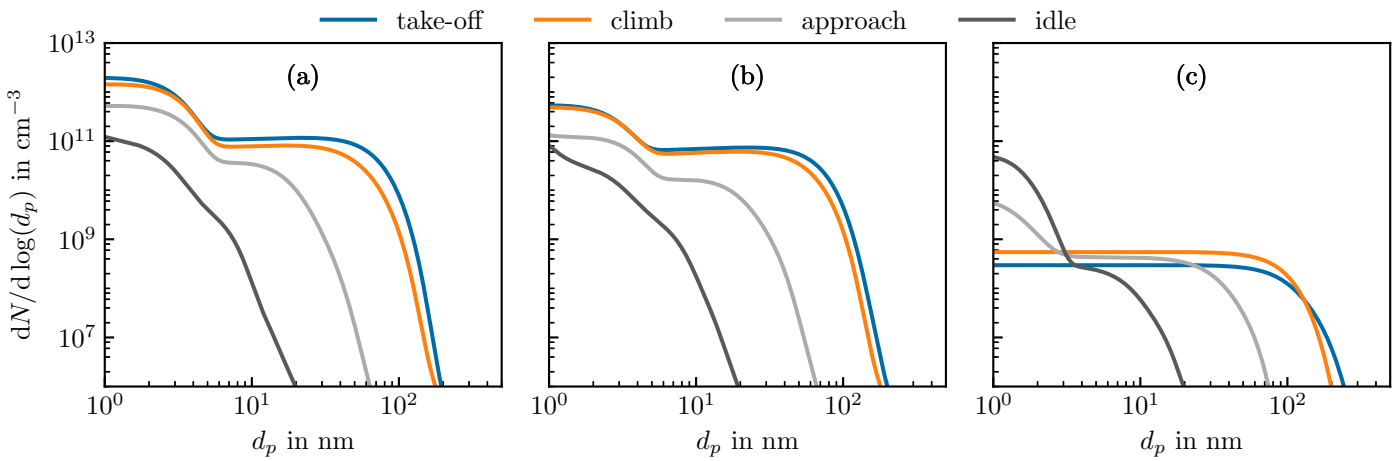

FIGURE 6: RECONSTRUCTED PSD IN THE RICH (a), QUENCH (b) AND LEAN (c) ZONE OF THE COMBUSTION CHAMBER FOR ALL FOUR OPERATING CONDITIONS.

between the gas and solid phase into account.

The general characteristics of the combustor follow the RQL concept with a rich primary zone, fast quenching through mixing with fresh air, and a following lean region. Transient flow phenomena caused by geometrical features of the combustion chamber influence the mixing in the reaction zone and lead to an asymmetric flow and mixing field. The soot emissions at the exit of the combustion chamber are compared to certification measurements of the emission index EI_{mass}. Good agreement with the measurement for the engine certification is achieved at all four operating conditions. The trend and magnitude are reproduced well, and only the soot emission index at the take-off condition is underestimated. Large fluctuations of up to one order of magnitude are observed for the two highest load cases, take-off and climb, demonstrating the importance of time-resolved simulations for accurate soot prediction.

Furthermore, the soot PSD was reconstructed inside an aero-engine combustor for the first time. For all operating conditions, the peak of small particles is found in the rich primary reaction zone where PAHs are present, leading to the formation of the first nucleated soot particles. Particle growth processes lead to the formation of particles with larger diameters and the maximum particle size increases with higher thrust levels. In the quench and lean zones, the soot oxidation process reduces the particle number significantly, especially for the two highest load cases.

In summary, the simulations performed in this work have shown a good agreement with experimental data and provided a deeper insight into the soot evolution process inside a real aero-engine combustor. To further improve soot prediction, particle aggregation should be included in future works. Overall, the advanced models applied have produced promising results for complex fuels under realistic conditions. This is particularly relevant for future combustors powered by SAF, which, while carbon-neutral, may still produce soot with variable features depending on the aromatic contents [50]. Future works should evaluate various SAF using the proposed high-fidelity, fuel-flexible framework to enable a CFD-based design of new-generation low-emission aero-engines.

ACKNOWLEDGMENT

This research has been funded by the the Clean Sky 2 Joint Undertaking under the European Union's Horizon 2020 research and innovation program under the ESTiMatE project, Grant Agreement No. 821418, the European Union's Horizon 2020 research and innovation program under the Center of Excellence in Combustion project, grant agreement No. 952181 and the German Federal Ministry for Economics and Climate Action under the Federal Aeronautical Research Program (LuFo VI, Call 2) under grant 20D2102C. We acknowledge PRACE for awarding us access to HAWK at GCS@HLRS, Germany for the calculations.

REFERENCES

[1] European Commission, Directorate-General for Mobility and Transport, Directorate-General for Research and Innovation, 2012, *Fligthphath 2050 Europe's vision for aviation*. Publications Office, https://doi.org/10.2777/50266.

[2] Angersbach, A., Bestie, D. and Eggels, R., 2013, "Automated combustor preliminary design using tools of different fidelity", Proceedings of the ASME Turbo Expo, San Antonio, Texas, June 3–7, 2013, ASME Paper No. GT2013-94411, pp. 1–8, https://doi.org/10.1115/GT2013-94411.

[3] Eggels, R. L. G. M., 2018, "The Application of Combustion LES Within Industry.", Direct and Large-Eddy Simulation X, Grigoriadis, Dimokratis G.E., Geurts, Bernard J., Kuerten, Hans, Fröhlich, Jochen and Armenio, Vincenzo, Springer International Publishing, pp. 3–13. 2018.

[4] Leung, K. M., Lindstedt, R. P. and Jones, W. P., 1991, "A simplified reaction mechanism for soot formation in

nonpremixed flames", *Combustion and Flame* 87(3-4), pp. 289–305, https://doi.org/10.1016/0010-2180(91)90114-Q.

[5] Brocklehurst, H. T., Priddin, C. H. and Moss, J. B., 1997 "Soot Predictions Within an Aero Gas Turbine Combustion Chamber", Proceedings of the ASME 1997 International Gas Turbine and Aeroengine Congress and Exhibition. Volume 2: Coal, Biomass and Alternative Fuels; Combustion and Fuels; Oil and Gas Applications; Cycle Innovations, Orlando, Florida, USA, June 2—5, 1997, https://doi.org/10.1115/97-GT-148.

[6] Tolpadi, A. K., Danis, A. M., Mongia, H. C. and Lindstedt, R. P., 1997, "Soot Modeling in Gas Turbine Combustors", Proceedings of the ASME 1997 International Gas Turbine and Aeroengine Congress and Exhibition. Volume 2: Coal, Biomass and Alternative Fuels; Combustion and Fuels; Oil and Gas Applications; Cycle Innovations, Orlando, Florida, USA, June 2—5, 1997, https://doi.org/10.1115/97-GT-149.

[7] Barths, H, Peters, N, Brehm, N, Mack, A, Pfitzner, M and Smiljanovski, V., 1998, "Simulation of pollutant formation in a gas-turbine combustor using unsteady flamelets", *Symposium (International) on Combustion* 27(2), pp. 1841–1847, https://doi.org/10.1016/S0082-0784(98)80026-X.

[8] Balthasar, M., Mauss, F., Pfitzner, M. and Mack, A., 2002, "Implementation and validation of a new soot model and application to aeroengine combustors", *ASME J Eng Gas Turbines Power* 124(1), pp. 66–74. https://doi.org/10.1115/1.1377596.

[9] Riesmeier, E., Honnet, S. and Peters, N., 2004, "Flamelet Modeling of Pollutant Formation in a Gas Turbine Combustion Chamber Using Detailed Chemistry for a Kerosene Model Fuel", *ASME J Eng Gas Turbines Power* 126(4), pp. 899–905. https://doi.org/10.1115/1.1787507.

[10] Moss, J. B. and Aksit, I. M., 2007, "Modelling soot formation in a laminar diffusion flame burning a surrogate kerosene fuel", *Proceedings of the Combustion Institute*, 31 II(2), pp. 3139–3146. https://doi.org/10.1016/j.proci.2006.07.016.

[11] Saffaripour, M., Veshkini, A., Kholghy, M. and Thomson, M. J., 2014, "Experimental investigation and detailed modeling of soot aggregate formation and size distribution in laminar coflow diffusion flames of Jet A-1, a synthetic kerosene, and n-decane", *Combustion and Flame* 161(3), pp. 848–863. https://doi.org/10.1016/j.combustflame.2013.10.016.

[12] Zettervall, N., Fureby, C. and Nilsson, E. J. K., 2020, "A reduced chemical kinetic reaction mechanism for kerosene-air combustion", *Fuel* 269, p. 117446, https://doi.org/10.1016/j.fuel.2020.117446.

[13] Mueller, M. E. and Pitsch, H., 2013, "Large eddy simulation of soot evolution in an aircraft combustor", *Physics of Fluids*, 25(11), https://doi.org/10.1063/1.4819347.

[14] Eigentler, F., Gerlinger, P. and Eggels, R., "Soot CFD simulation of a real aero engine combustor", AIAA Science and Technology Forum and Exposition, AIAA SciTech Forum 2022, San Diego, CA, https://doi.org/10.2514/6.2022-0489.

[15] Janicka, J. and Sadiki, A., 2005, "Large eddy simulation of turbulent combustion systems", *Proceedings of the Combustion Institute* 30(1), pp. 537–547, https://doi.org/10.1016/j.proci.2004.08.279.

[16] van Oijen, J. A. and de Goey, L. P. H., 2000, "Modelling of premixed laminar flames using flamelet-generated manifolds", *Combustion Science and Technology* 161(1), pp. 113–137, https://doi.org/10.1080/00102200008935814.

[17] Zucca, A., Marchisio, D. L., Barresi, A. A. and Fox, R. O., 2006, "Implementation of the population balance equation in CFD codes for modelling soot formation in turbulent flames", *Chemical Engineering Science* 61(1), pp. 87–95, https://doi.org/10.1016/j.ces.2004.11.061.

[18] Attili, A., Bisetti, F., Mueller, M. E. and Pitsch, H., 2014 "Formation, growth, and transport of soot in a three-dimensional turbulent non-premixed jet flame", *Combustion and Flame* 161(7), pp. 1849–1865, https://doi.org/10.1016/j.combustflame.2014.01.008.

[19] Mueller, M. E. and Pitsch, H., 2012, "LES model for sooting turbulent nonpremixed flames", *Combustion and Flame* 159(6), pp. 2166–2180, https://doi.org/10.1016/j.combustflame.2012.02.001.

[20] Xuan, Y. and Blanquart, G., 2015, "Effects of aromatic chemistry-turbulence interactions on soot formation in a turbulent non-premixed flame", *Proceedings of the Combustion Institute* 35(2), pp. 1911–1919, https://doi.org/10.1016/j.proci.2014.06.138.

[21] Koo, H., Hassanaly, M., Raman, V., Mueller, M. E. and Geigle, K. P., 2017, "Large-Eddy Simulation of Soot Formation in a Model Gas Turbine Combustor", *ASME J Eng Gas Turbines Power* 139(3), pp. 1–9, https://doi.org/10.1115/1.4034448.

[22] Hausdorff, F., 1923, "Momentprobleme für ein endliches Intervall", *Mathematische Zeitschrift* 16(1), pp. 220–248, https://doi.org/10.1007/BF01175684.

[23] Shohat, J. and Tamarkin, J., 1943, "The Problem of Moments", Vol. 1 of *Mathematical Surveys and Monographs*, American Mathematical Society, https://doi.org/10.1090/surv/001.

[24] Salenbauch, S., Hasse, C., Vanni, M. and Marchisio, D. L., 2018, "A numerically robust method of moments with number density function reconstruction and its application to soot formation, growth and oxidation", *Journal of Aerosol Science* 128, pp. 34–49, https://doi.org/10.1016/j.jaerosci.2018.11.009.

[25] Yuan, C., Laurent, F. and Fox, R. O., 2012 "An extended quadrature method of moments for population balance equations", *Journal of Aerosol Science* 51, pp. 1–23, https://doi.org/10.1016/j.jaerosci.2012.04.003.

[26] Wick, A., Nguyen, T. T., Laurent, F., Fox, R. O. and Pitsch, H., 2017, "Modeling soot oxidation with the Extended Quadrature Method of Moments", *Proceedings*

of the Combustion Institute 36(1), pp. 789–797, https://doi.org/10.1016/j.proci.2016.08.004.

[27] Pigou, M., Morchain, J., Fede, P., Penet, M. I. and Laronze, G., 2018, "New developments of the Extended Quadrature Method of Moments to solve Population Balance Equations", *Journal of Computational Physics* 365, pp. 243–268, https://doi.org/10.1016/j.jcp.2018.03.027.

[28] Nguyen, T. T., Laurent, F., Fox, R. O. and Massot, M., 2016, "Solution of population balance equations in applications with fine particles: Mathematical modeling and numerical schemes", *Journal of Computational Physics* 325, pp. 129–156, https://doi.org/10.1016/j.jcp.2016.08.017.

[29] Ferraro, F., Gierth, S., Salenbauch, S., Han, W. and Hasse, C., 2022, "Soot particle size distribution reconstruction in a turbulent sooting flame with the split-based extended quadrature method of moments", *Physics of Fluids* 34(7), https://doi.org/10.1063/5.0098382.

[30] Çokuslu, Ö. H., Hasse, C., Geigle, K. P. and Ferraro, F., 2022, "Soot prediction in a Model Aero-Engine Combustor using a Quadrature-based method of moments", AIAA Science and Technology Forum and Exposition, AIAA SciTech Forum 2022, San Diego, CA, https://doi.org/10.2514/6.2022-1446.

[31] Brehm, N., Baker, S. J. and Jones, S. P., 1997, "A three step NOx reduction programme: "Achievements with the single annular low-NOx combustor for the BR 700 engine family"", Proceedings of the ASME 1997 International Gas Turbine and Aeroengine Congress and Exhibition. Volume 2: Coal, Biomass and Alternative Fuels; Combustion and Fuels; Oil and Gas Applications; Cycle Innovations, Orlando, Florida, USA, June 2—5, 1997, https://doi.org/10.1115/97-GT-145.

[32] Smiljanovski, V. and Brehm, N., 1999, "CFO liquid spray combustion analysis of a single annular gas turbine combustor", Proceedings of the ASME 1999 International Gas Turbine and Aeroengine Congress and Exhibition. Volume 2: Coal, Biomass and Alternative Fuels; Combustion and Fuels; Oil and Gas Applications; Cycle Innovations, Indianapolis, Indiana, USA, June 7–10, 1999, https://doi.org/10.1115/99-GT-300.

[33] Anand, M. S., Eggels, R., Staufer, M., Zedda, M. and Zhu, J., 2013, "An Advanced Unstructured-Grid Finite-Volume Design System for Gas Turbine Combustion Analysis", Proceedings of the ASME 2013 Gas Turbine India Conference, ASME 2013 Gas Turbine India Conference, Bangalore, Karnataka, India, December 5–6, 2013, https://doi.org/10.1115/GTINDIA2013-3537.

[34] Jasak, H., Weller, H. G. and Gosman, A. D., 1999, "High resolution NVD differencing scheme for arbitrarily unstructured meshes", *International Journal for Numerical Methods in Fluids* 31(2), pp. 431–449, https://doi.org/10.1002/(sici)1097-0363(19990930)31:2<431::aid-fld884>3.3.co;2-k.

[35] Nicoud, F., Toda, Hubert Baya, Cabrit, O., Bose, S. and Lee, J., 2011, "Using singular values to build a subgrid-scale model for large eddy simulations", *Physics of Fluids* 23(8), https://doi.org/10.1063/1.3623274.

[36] Chin, J. S. and Lefebvre, A. H., 1983, "Steady-state evaporation characteristics of hydrocarbon fuel drops", *AIAA Journal* 21(10), pp. 1437–1443, https://doi.org/10.2514/3.8264.

[37] Hermanns, R., 2001, "CHEM1D, a one-dimensional laminar flame code." Report, Eindhoven University of Technology.

[38] Ramirez Hernandez, A., Kathrotia, T., Methling, T., Braun-Unkhoff, M. and Riedel, U., 2022, "Reaction Model Development of Selected Aromatics as Relevant Molecules of a Kerosene Surrogate—The Importance of m -Xylene Within the Combustion of 1,3,5-Trimethylbenzene", *ASME J Eng Gas Turbines Power* 144(2), pp. 1–8, https://doi.org/10.1115/1.4052206.

[39] Ramirez Hernandez, A., Kathrotia, T., Methling, T., Braun-Unkhoff, M. and Riedel, U., 2022, "An Upgraded Chemical Kinetic Mechanism for ISO-Octane Oxidation: Prediction of Polyaromatics Formation in Laminar Counterflow Diffusion Flames", Proceedings of the ASME Turbo Expo 2022: Turbomachinery Technical Conference and Exposition, Volume 2: Coal, Biomass, Hydrogen, and Alternative Fuels; Controls, Diagnostics, and Instrumentation; Steam Turbine, Rotterdam, Netherlands, June 13–17, 2022, https://doi.org/10.1115/GT2022-83053.

[40] Kathrotia, T., Oßwald, P., Naumann, C., Richter, S. and Köhler, M., 2021, "Combustion kinetics of alternative jet fuels, Part-II: Reaction model for fuel surrogate", *Fuel* 302, p. 120736, https://doi.org/10.1016/j.fuel.2021.120736.

[41] Sewerin, F. and Rigopoulos, S., 2018, "An LES-PBE-PDF approach for predicting the soot particle size distribution in turbulent flames", *Combustion and Flame* 189, pp. 62–76, https://doi.org/10.1016/j.combustflame.2017.09.045.

[42] Balthasar, M. and Kraft, M., 2003, "A stochastic approach to calculate the particle size distribution function of soot particles in laminar premixed flames", *Combustion and Flame* 133(3), pp. 289–298, https://doi.org/10.1016/S0010-2180(03)00003-8.

[43] Kazakov, A. and Frenklach, M., 1998, "Dynamic modeling of soot particle coagulation and aggregation: Implementation with the method of moments and application to high-pressure laminar premixed flames", *Combustion and Flame* 114(3-4), pp. 484–501, https://doi.org/10.1016/S0010-2180(97)00322-2.

[44] Frenklach, M. and Wang, H., 1991, "Detailed modeling of soot particle nucleation and growth", *Symposium (International) on Combustion* 23(1), pp. 1559–1566, https://doi.org/10.1016/S0082-0784(06)80426-1.

[45] Frenklach, M. and Wang, H., 1994, *Detailed Mechanism and Modeling of Soot Particle Formation*, Soot Formation in Combustion, Springer Series in Chemical Physics, vol 59,

Bockhorn, H., Springer, Berlin, Heidelberg, pp. 165–192, https://doi.org/10.1007/978-3-642-85167-4_10.

[46] Appel, J., Bockhorn, H. and Frenklach, M., 2004, "Kinetic modeling of soot formation with detailed chemistry and physics: Laminar premixed flames of C2 hydrocarbons", *Combustion and Flame* 121(1-2), pp. 122–136, https://doi.org/10.1016/S0010-2180(99)00135-2.

[47] Ihme, M. and Pitsch, H., 2008, "Prediction of extinction and reignition in nonpremixed turbulent flames using a flamelet/progress variable model. 2. Application in LES of Sandia flames D and E", *Combustion and Flame* 155(1-2) pp. 90–107, https://doi.org/10.1016/j.combustflame.2008.04.015.

[48] Celik, I. B., Cehreli, Z. N. and Yavuz, I., 2005, "Index of Resolution Quality for Large Eddy Simulations", *Journal of Fluids Engineering* 127(5), pp. 949–958, https://doi.org/10.1115/1.1990201.

[49] EASA, 2022, "ICAO aircraft engine emissions databank", accessed December 22, 2022, https://www.easa.europa.eu/en/domains/environment/icao-aircraft-engine-emissions-databank.

[50] Kumal, R. R., Liu, J., Gharpure, A., Vander Wal, R. L., Kinsey, J. S., Giannelli, B., Stevens, J., et al., 2020, "Impact of Biofuel Blends on Black Carbon Emissions from a Gas Turbine Engine", *Energy & Fuels* 34(4), pp. 4958–4966, https://doi.org/10.1021/acs.energyfuels.0c00094.

